

Method to optimize an additively-manufactured functionally-graded lattice structure for effective liquid cooling



Akihiro Takezawa^{a,*}, Xiaopeng Zhang^{b,a}, Masaki Kato^c, Mitsuru Kitamura^a

^a Department of Transportation and Environmental Systems, Graduate school of Engineering, Hiroshima University, 1-4-1 Kagamiyama, Higashi-Hiroshima, Hiroshima 739-8527, Japan

^b State Key Laboratory of Structural Analysis for Industrial Equipment, Dalian University of Technology, Dalian 116024, China

^c Aichi Center for Industry and Science Technology, 1267-1 Akiai, Yakusa-cho, Toyota, Aichi 470-0356, Japan

ARTICLE INFO

Keywords:

Lattice density optimization
Darcy–Forchheimer law
Brinkman–Forchheimer equation
Additive manufacturing
Thermal conduction-convection

ABSTRACT

The development of cooling devices is important for many industrial products, and the lattice structure fabricated by additive manufacturing is expected to be useful for effective liquid cooling. However, lattice density should be carefully designed for an effective arrangement of coolant flow. In this research, we optimize the lattice density distribution using a lattice structure approximation and the gradient method. Fluid flow is approximated by deriving effective properties from the Darcy–Forchheimer law and analyzing the flow according to the Brinkman–Forchheimer equation. Thermal conduction and convection are also approximated as a weakly coupled problem. We use a simple basic lattice shape composed of pillars, optimizing only its density distribution by setting the pillar diameter as the design variable. Steady-state pressure and temperature reductions are treated as multi-objective functions. Through 2D and 3D numerical studies, we discuss the validity and limitations of the proposed method. Although observable errors in accuracy exist between the results obtained from the optimization and full scale models, relative performance optimization was considered successful.

1. Introduction

Effective cooling or heat exchange is a general engineering issue in various industrial products. Developing innovative device shapes is a solution to this issue. Until recently, the limitations of fabrication technology made it difficult to realize complicated geometries. However, additive manufacturing (AM) [1] facilitates an innovative 3D layer-by-layer construction of objects. Although these technologies originated with photopolymers and thermoelastic polymers, metals have also been recently used in AM. AM achieves sufficient thermal conductivity in the cooling device of the final product itself, not just in the prototype. Thus, the use of AM has recently become widespread in the development of innovative liquid-cooling geometries.

A basic geometry realized only by AM is a 3D structure with inner air holes, termed a “lattice structure.” This construction achieves effective cooling by allowing coolant to flow to the air holes [2,3]. Since heat exchange depends on the lattice geometry, any attempt at structural optimization focuses on designing complicated structures. For non-lattice AM cooling devices, several design optimizations have been reported [4–6].

There are two aspects to lattice structure optimization. The first is

the optimization of the geometry of the lattice unit cell. Topology optimization (TO), which is a form of structural optimization, enables the formation of refined structures via topological changes (the number of holes) [7,8], and provides the most fundamental performance improvement for the lattice unit cell. In designing a lattice, macroscopic lattice properties are treated as objective functions. Recent studies report developing innovative lattice shapes by a combination of TO and AM, that exhibit a stiffness and permeability matching those of human bone [9]. Further, these same studies report maximized or improved stiffness and strength [10,11], maximized thermal conductivity [12], a negative Poisson ratio [13–15], a negative or extra-large thermal expansion [16,17], and a negative or zero compressibility [18].

The second aspect is optimizing the lattice density distribution. One advantage of the AM lattice structure is a variable lattice shape, whose structural, thermal, and other related performance characteristics depend on location-similar to the dependence displayed by functionally graded materials [19]. TO originally involved optimizing the density distribution of a composite of a material and air [7,8]. Thus, a TO algorithm can also be used to optimize the lattice density distribution. This was first applied in the design of artificial bones [20] and was extended to maximizing stiffness or strength [21–23], improving anti-

* Corresponding author.

E-mail address: akihiro@hiroshima-u.ac.jp (A. Takezawa).

buckling performance [24], improving vibration characteristics [25,26], and maximizing thermal conductivity [27,28].

Both of the above aspects are important in designing an effective lattice structure. In designing heat-exchange lattice structures, two physical problems have to be considered: coolant flow, as well as the transmission of heat through the lattice by conduction and convection. While heat conduction has already been discussed in terms of unit lattice design and lattice density distribution [12,27,28], there are still unsolved problems surrounding fluid flow. Although studies on TO have reported on the design of lattice unit cells, they are limited to numerical studies [29–31]. In addition, these studies are based on Darcy's law, which is valid only for low Reynolds numbers, corresponding to viscosity-dominant very slow flow or flow over small scales. As a certain level of speed is required for effective heat exchange and a lattice unit cell fabricated using AM cannot be extremely small, such flows are not appropriate for effective cooling. Moreover, lattice density optimization for fluid flow is an open problem, even at slow speeds. Although TO has been widely used to design channels with Stokes, turbulent, and heat exchange flows [32–35], few studies focus on using the lattice density distribution for effective heat exchange devices.

As lattice drag becomes non-linear when the Reynolds number exceeds approximately 10 [36,37], Darcy's law does not work. However, its extension, the Darcy–Forchheimer law, considers drag through a porous medium as a quadratic function for Reynolds number up to the order of 10^2 [37]. Although this is a classical theory, recent experiments and simulations were performed for an AM lattice and a conventional porous material [38,39].

On this basis, we develop a method of optimizing the lattice density distribution for effective liquid cooling with a flow characterized by a Reynolds number up to the order of 10^2 . The basic lattice shape is simply composed of pillars, and only its distribution is optimized by setting the pillar diameter as the design variable. The Darcy permeability, Forchheimer quadratic drag, and effective thermal conductivity are calculated using the averaging theorem and the finite element method (FEM) for a representative lattice unit cell. Continuous functions related to the design variable and the effective properties are approximated by polynomials. The modeling of the weakly coupled fluid flow and thermal conduction-convection are treated as a steady-state problem and solved by the FEM. Inlet pressure and temperature reduction are treated as a weighted sum and are considered a multi-objective function. The design variable is optimized by the method of moving asymptotes (MMA) [40] under a lower-limit volume constraint. Through data gathered by 2D and 3D numerical studies, the validity and limitations of the proposed method are discussed.

2. Methods

2.1. Approximating fluid flow and heat transfer in lattice structure

To optimize fluid flow and thermal conduction-convection in a lattice structure, we have to simulate them in the target domain Ω which is entirely structured as a lattice. As shown in Fig. 1, an incompressible fluid with fixed temperature T_0 has a flow Γ_{in} into the domain from the inlet and flow Γ_{out} out from the outlet with zero pressure. A heat flux Γ_h is applied to the domain boundary, and other domains are regarded as thermally insulated.

To simulate the fluid flow inside a porous medium, we introduce the Darcy velocity vector $\mathbf{u} = [u, v, w]^T$, which is defined as the discharge per unit area, with units of length per time, where u , v , and w are xyz elements of \mathbf{u} . It represents an average or effective fluid velocity through the porous medium. By analogy with the flow through pipes, the transition from laminar to turbulent flow is represented by the Reynolds number Re . This is formulated as [36,37]:

$$Re = \frac{\rho|\mathbf{u}|d}{\mu}, \quad (1)$$

where ρ and μ are the mass density and dynamic viscosity of the fluid, respectively, and d is the representative diameter of the porous medium. When the porous Reynolds number is in the order of 10^2 , the pressure gradient of the flow through an isotropic porous medium is represented as [36,37,41]:

$$\nabla p = -\frac{\mu}{\kappa}\mathbf{u} - \frac{c_F\rho}{\sqrt{\kappa}}|\mathbf{u}|\mathbf{u}, \quad (2)$$

where κ and c_F are the permeability and form-drag constant of the porous medium, respectively, and $\sqrt{\kappa}$ is used as d in Eq. (1). When the Reynolds number is very low, the second term can be ignored and Eq. (2) represents Darcy's law. By analogy with the Navier–Stokes equation, the steady-state Darcy velocity distribution of the fluid through the porous medium can be formulated as follows [37,42–44]:

$$\frac{\rho}{\epsilon}\mathbf{u} \cdot \left(\nabla \frac{\mathbf{u}}{\epsilon} \right) = -\nabla P + \frac{\mu}{\epsilon\rho}\nabla^2\mathbf{u} - \frac{\mu}{\kappa}\mathbf{u} - \frac{c_F\rho}{\sqrt{\kappa}}|\mathbf{u}|\mathbf{u}, \quad (3)$$

where ϵ is the porosity of the porous medium. This is the Brinkman–Forchheimer equation.

Next, the temperature distribution is calculated using \mathbf{u} that is obtained by solving Eq. (3). This can be calculated from the conventional thermal conduction–convection equation,

$$\rho C_p \mathbf{u} \cdot \nabla T - \lambda^* \nabla^2 T = Q, \quad (4)$$

where C_p is the fluid heat capacity at constant pressure and λ^* is the effective thermal conduction coefficient of the fluid-filled porous medium.

2.2. Calculation of effective physical properties of the lattice

To solve Eqs. (3) and (4), we must calculate the effective physical properties of the porous medium, which are the permeability κ , form-drag constant c_F , and the thermal conductivity λ . They are calculated by using the averaging theorem [45,46]. In this method, the porous medium is assumed to be statistically homogeneous (SH), i.e., in a representative volume element (RVE) with volume Ω_μ , it is assumed to be macroscopically homogeneous. This SH field in the RVE is generated by introducing boundary conditions that produce a homogeneous field if the body is a bulk material. The effective properties are calculated from the average response in Ω_μ under SH field boundary conditions.

Initially, κ and c_F are calculated. A unit lattice composed of a fluid and a solid domain is governed by the conventional Navier–Stokes equation. The isotropies of κ and c_F are guaranteed by assuming an orthogonal symmetry of the unit lattice. We set pressure boundary conditions on any one pair of opposite faces and periodic boundary conditions on the other two pairs of opposite faces, (as shown in Fig. 2(a)). This produces an SH pressure field in a single direction. After calculating the pressure drops and Darcy velocities through the lattice at several pressure values, we plot a graph of the pressure drop versus the Darcy flow. From the coefficients of the quadratic approximation of the distribution, we calculate κ and c_F .

The effective thermal conductivity is also calculated by considering thermal conduction in the same geometry. From the Fourier law $\mathbf{j} = -\lambda \nabla T$, the heat flux \mathbf{j} is proportional to the temperature gradient ∇T , the coefficient of which is thermal conductivity. By setting the SH temperature field with a unit temperature gradient as shown in Fig. 2 (b), and solving the thermal conductivity problem, the effective thermal conductivity λ^* is calculated as the average of $-\lambda \nabla T$ over the RVE domain.

2.3. Optimization of the lattice density distribution

The lattice density distribution is optimized over the target domain

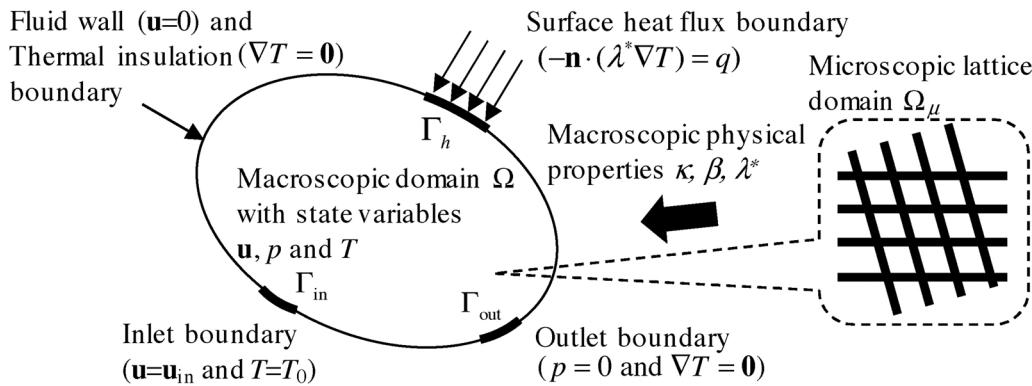


Fig. 1. Outline of the design target domain and boundary conditions.

Ω . This optimization process can use nearly the same algorithm as TO [7,8]. The fundamental concept in TO is the optimization of the 0–1 discrete function distribution that represents the amount of material at each position. However, a discrete function distribution on a continuum field is mathematically ill-posed [47]. To resolve this, homogenization is used, which relaxes the solution space from discrete to continuum [7,47]. This replaces the original material distribution optimization with an optimization of the volume fraction of a composite consisting of the original material and a material with very low physical properties. Thus, although the basic use of TO is in the generation of a structural topology, it is fundamentally the same as optimizing the lattice density distribution.

In conventional TO, an intermediate density from 0 to 1 should be avoided; the method known as simple isotropic material with penalization (SIMP) is used to penalize it because the density distribution is approximated by the 0–1 discrete function, and it is difficult to identify an intermediate value as 0 or 1. However, in lattice optimization, such intermediate value of the density function can be regarded as a lattice effective density with corresponding geometry. Thus, penalizing the intermediate density is not required. However, the physical properties of a lattice corresponding to the specified intermediate density must be prepared before optimization. In this research, physical properties with representative densities are derived and interpolated with polynomial functions. This is the most commonly used approach in deriving the effective properties of a lattice density distribution [21,25,27]. The lattice diameter is set as a function of the design variable d and mapped into the interval [0, 1].

Based on the above discussion, the optimization problem is formulated as follows:

$$\text{minimize}_d f(d) = w \ln \frac{1}{\Gamma_{\text{in}}} \int_{\Gamma_{\text{in}}} P d\Gamma + (1 - w) \ln \frac{1}{\Gamma_h} \int_{\Gamma_h} T d\Gamma, \quad (5)$$

subject to

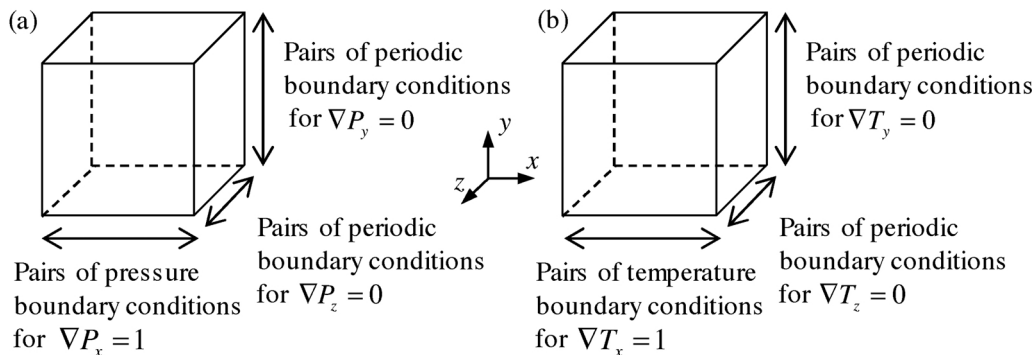


Fig. 2. SH boundary conditions of RVE for calculating effective lattice properties of (a) the permeability and form-drag constant and (b) the effective thermal conductivity.

Eqs. (3) and (4)

$$\int_{\Omega} (1 - \epsilon) dV \geq V^L \quad (6)$$

$$0 \leq d \leq 1, \quad (7)$$

where $w(1e0)$ is a weighting coefficient and V^L is the lower boundary of the total lattice volume. The objective function is the minimization of the weighted sum of the average fluid pressure of the inlet and average temperature of the heat flux boundary. A natural logarithm is introduced to adjust the order of each function and is effective for the multi-objective optimization of the positive value functions [34]. The lower constraint for the total lattice volume is based on TO research on cooling channels [34]. Moreover, in the case of a cooling device that requires a certain degree of stiffness such as a casting die, the lower limit of the total volume should aid in obtaining it.

2.4. Lattice shape and interpolation functions of effective properties

In this research, we introduce the simple shapes as shown in Fig. 3 as basic lattice geometries. For the 2D problem, the lattice is composed of a solid circle at the center of the square domain, and for the 3D problem it consists of a set of three orthogonal solid pillars at the center of the cubic fluid domain. The diameters of the circle and pillars are updated during the optimization. The length of the lattice unit cell is assumed to be 5 mm, and the pillar diameters are varied from $D = 1.0$ to 4.0 mm. The fluid and solid are assumed to be water and carbon steel with constant properties as shown in Table 1. The temperature dependence of the properties is ignored.

Next, the effective properties of these lattices are calculated as functions of the design variable. The diameter D ($1.0 \leq D \leq 4.0$) is mapped into the design variable d ($0 \leq d \leq 1$) by the equation $D = 1.0 + 3.0d$. Representative effective properties are calculated for the pillar with $D = 1.0$ to 4.0 mm with 0.5 mm intervals. They are then

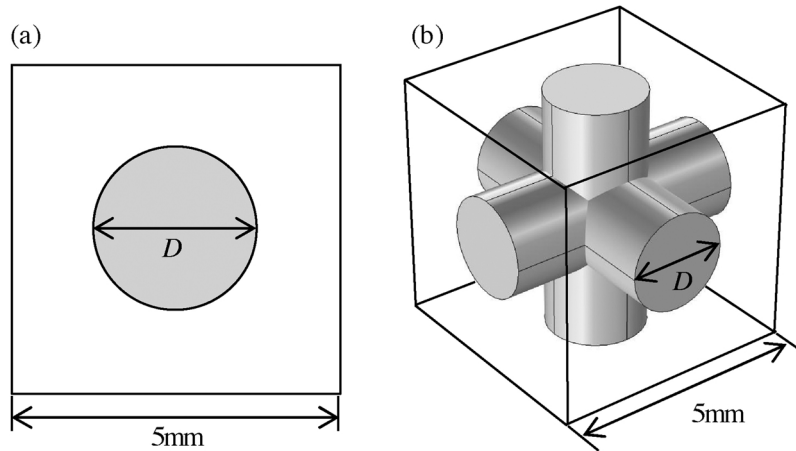


Fig. 3. Basic shapes of the unit lattices. (a) 2D case. (b) 3D case.

Table 1
Properties of materials used in this research.

	Mass density [kg/m ³]	Dynamic viscosity [kg/(m·s)]	Specific heat [J/(g·K)]	Thermal conductivity [W/(m·K)]
Liquid (Water)	1000	0.001	4200	0.6
Solid (Carbon steel)	Not used	Not used	Not used	53

interpolated with polynomial functions with respect to d .

The porosity ϵ is directly obtained geometrically. The effective thermal conductivity is calculated from an FEM analysis with the boundary conditions shown in Fig. 2 (b). These interpolation functions are shown in Fig. 4. The reason the thermal conductivity interpolation functions are markedly different for the 2D and 3D cases is the extent of the connectivity of the solid section of the lattice with the neighboring cells.

The cell permeability and form-drag coefficient are calculated from the relationship between the pressure drop and Darcy velocity in Eq. (2). The relationship between the $\frac{\partial p}{\partial x}$ and u obtained in the $D = 2.5$ mm cell is shown in Fig. 5 for the 2D and 3D cases. By comparing the coefficients of the interpolation functions with Eq. (2), the permeability κ and form-drag coefficient C_F are calculated. For simplicity, all the coefficients of the quadratic term of (2) are handled as a function of the design variable by introducing the symbol $\beta = \frac{C_F}{\sqrt{\kappa}}$. The interpolation functions of κ and β are shown in Fig. 6. We then checked the validities of the derived permeability and form-drag coefficient. The pressure drops were calculated using Eq. (2) with the interpolations for several lattice diameters shown in Fig. 5. These values were compared with a

conventional approximation [48], and the results show that the methods are consistent. Details are shown in Appendix A.

2.5. Optimization algorithm

The design variable is updated using a gradient-based algorithm. Fig. 7 provides a flowchart of the optimization procedure. The Darcy velocity, pressure, and temperature distribution in the target domain are calculated by solving the Brinkman–Forchheimer equation (3), and the thermal conduction-convection equation (4) through the application of FEM. Next, the objective function, which is the weighted sum of the average pressure and temperature, and the constraint on domain volume are calculated using Eqs. (5) and (6), respectively. The sensitivities for the objective function and constraint are also calculated using the adjoint variable method [49]. Finally, the design variables are updated by the MMA. These steps are repeated until the iteration limit or specified convergence criteria are reached.

3. Results

The validity and utility of the proposed method are confirmed with 2D and 3D examples. All FEM calculations are performed using the software COMSOL Multiphysics. All finite-element formulations are linear Lagrange elements. Residual minimization for the non-linear Brinkman–Forchheimer equation is performed by the Newton method. At the inlet, we fixed Darcy velocity and fixed temperature $T = 0$ °C. At the outlet, a fixed pressure $p = 0$ Pa is assumed.

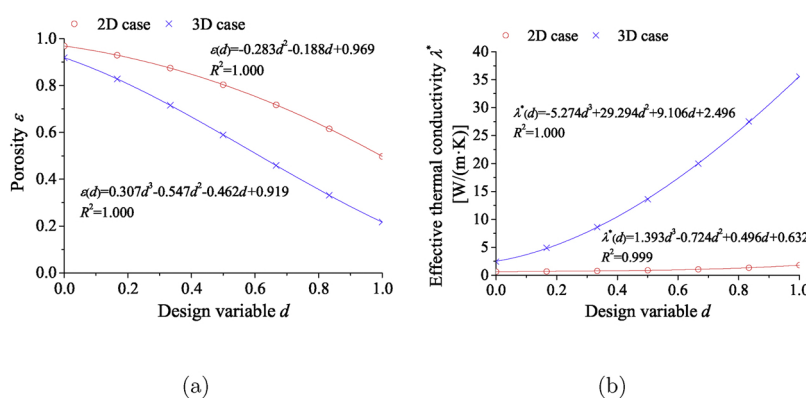


Fig. 4. Interpolation functions of (a) porosity and (b) effective thermal conductivity with respect to the design variable.

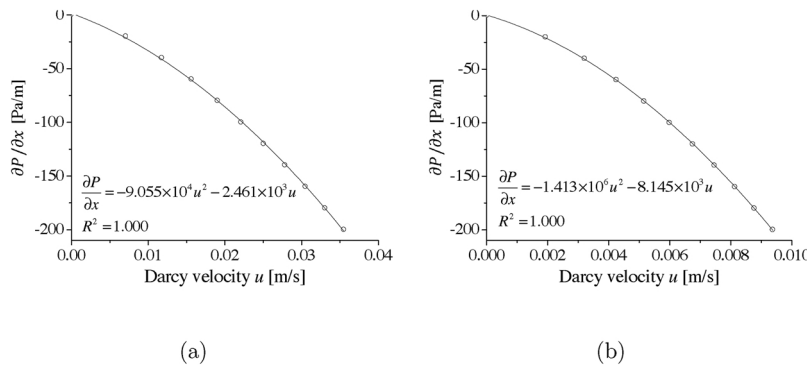


Fig. 5. Interpolation functions of pressure gradient with respect to Darcy velocity in (a) 2D and (b) 3D lattice with $D = 2.5$ mm.

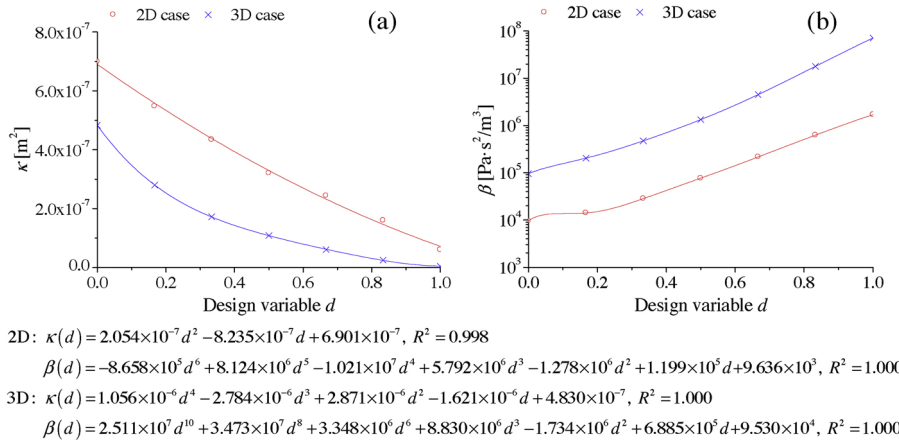


Fig. 6. Interpolation functions of (a) permeability and (b) coefficient of the quadratic term of Eq. (2).

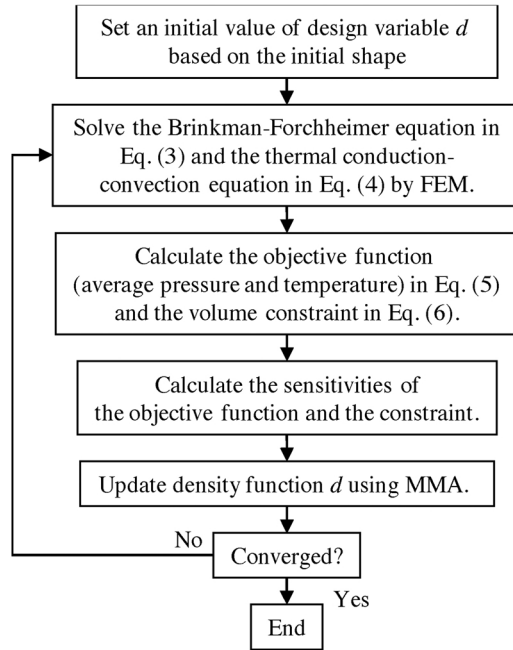


Fig. 7. Flowchart of optimization procedure.

3.1. 2D example

Regarding the 2D examples, a domain composed of a square lattice and two rectangular inlet and outlet fluid domains shown in Fig. 8 were used. The 100-mm lattice domain square is divided into a lattice with 5-

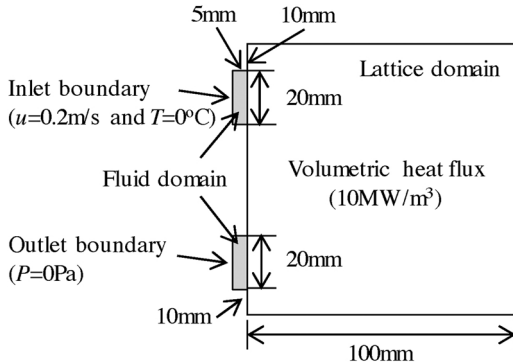


Fig. 8. Analysis domain of 2D numerical example.

mm spacings. Thus, the number of lattices is 400, which is equal to the number of design variables. The thickness of the domain is assumed to be 1 m, which is sufficiently large for the 2D approximation. The flow is U-shaped with one inlet and one outlet on the same side. The inlet Darcy velocity is set to 0.2 m/s. A uniform volume heat flux of 10 MW/m³ was applied to the entire domain. The objective function considers the average water pressure at the inlet and the average temperature of the lattice domain. The lower volume limit is 30% of the volume of the fully dense lattice domain. The initial shape is a uniform lattice with 30% volume fraction and 3.1 mm diameter. Weight w in the objective function of Eq. (5) is varied from 0 to 1 in intervals of 0.1.

The convergence histories of $w = 0.0, 0.5$, and 1.0 in Fig. 9 show smooth convergences. Fig. 10 shows pressure and temperature distributions of optimal solutions after 50 iterations. Volume constraints were active in all results. A clear trade-off was observed between both the criteria. Fig. 11 shows the initial and optimal diameter distributions

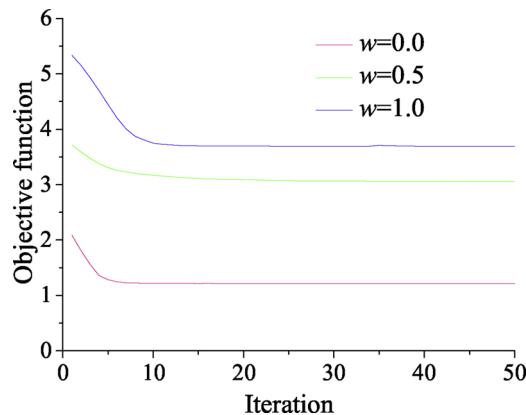


Fig. 9. Convergence history of objective functions for the 2D example for the $w = 0$, 0.5, and 1.0 cases.

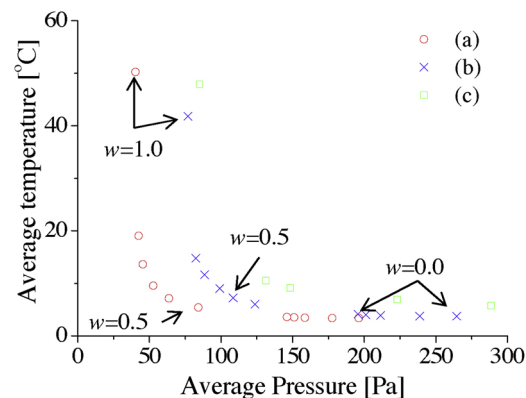


Fig. 10. Pareto front of the 2D example. (a) Optimal results of the Brinkman–Forchheimer model. (b) Re-analysis results by the full scale Navier–Stokes model of (a). (c) Re-analysis results by the full scale Navier–Stokes model of the optimal results obtained by ignoring quadratic drag term.

and the corresponding detailed geometries for the $w = 0.0$, 0.5, and 1.0 cases. The maximum Reynolds numbers in Eq. (1) are 231, 191, and 189 for $w = 0.0$, 0.5, and 1.0, respectively, as calculated from the local Darcy velocity and permeability. For $w = 0.0$, the path between the inlet and outlet is blocked by a dense lattice to provide water flow to the whole domain, and it is opened for $w = 1.0$. The result for $w = 0.5$ has both shortcut and roundabout paths, showing an intermediate performance in temperature reduction and low-pressure loss. Figs. 12 and 13 show the pressure distributions and streamlines of the Brinkman–Forchheimer model for the initial geometry and each optimal result. Results with high-pressure loss, the initial geometry, and the $w = 0$ result, show high pressure concentration near the inlet. Another two results show relatively uniform pressure distributions. Streamlines show the water flow paths form for low-density lattices. Even the initial uniform lattice shows flow covering a relatively wide domain area while pressure loss is high. For $w = 1.0$, fluid flow occurs between the inlet and outlet. For $w = 0$ and 0.5, the combination of dense and sparse lattices generates wide flow. In this optimization setting, water leaks out when the set of dense lattices is small. If the shortcut flow is included, pressure loss can be reduced by sacrificing temperature reduction. Other characteristic geometries shown for $w = 0.0$ and 0.5 are isolated paths on dense lattices. Although they look like dead-ends, they may contribute to gathering of small flows that leak from dense lattices. Fig. 14 shows the temperature distribution of the Brinkman–Forchheimer model for the initial geometry and each optimal result. A wider flow area reduces the temperature further.

Every result was re-analyzed using the full scale Navier–Stokes and thermal conduction-convection models. The calculated pressure and temperature are plotted in Fig. 10 together with the Brinkman–Forchheimer results. Although the errors between these models are 35.6% for pressure and 12.9% for temperature on average, the relative performance can be compared using the Brinkman–Forchheimer model because the inferior-to-superior relationship of each result is identical in both models. Fig. 15 shows the pressure, velocity magnitude and temperature distributions of the full scale model for $w = 0.5$. Although values were different from those of the Brinkman–Forchheimer model, the distributions were similar in both the models. This is the reason that

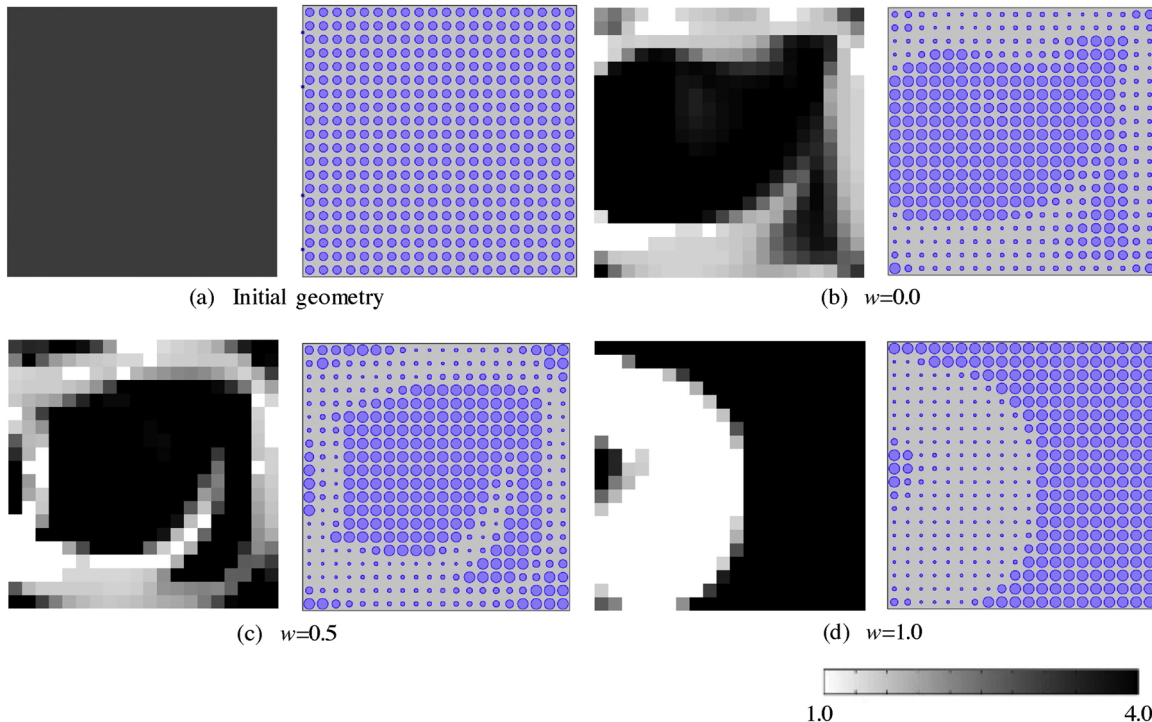


Fig. 11. Optimal diameter distributions and corresponding geometries of the 2D example.

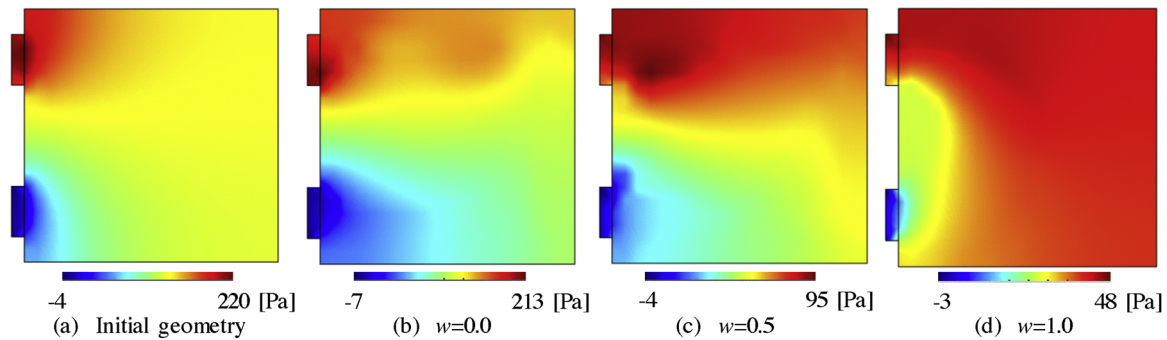


Fig. 12. Pressure distributions of optimal results of the 2D example.

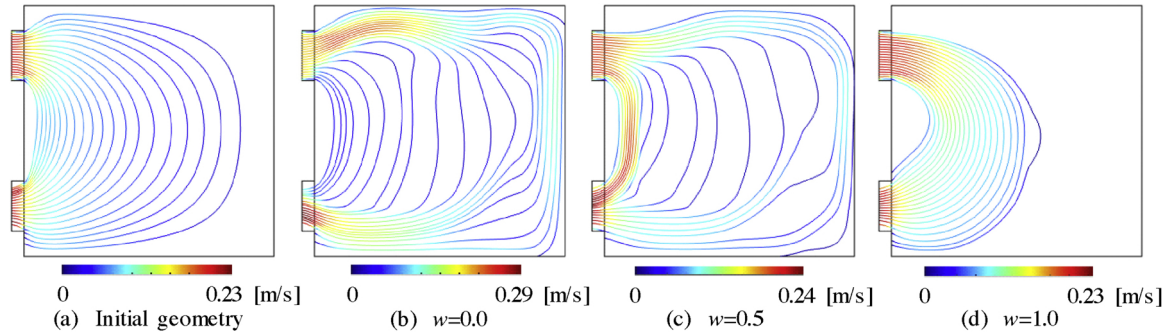


Fig. 13. Stream lines of the optimal results of the 2D example.

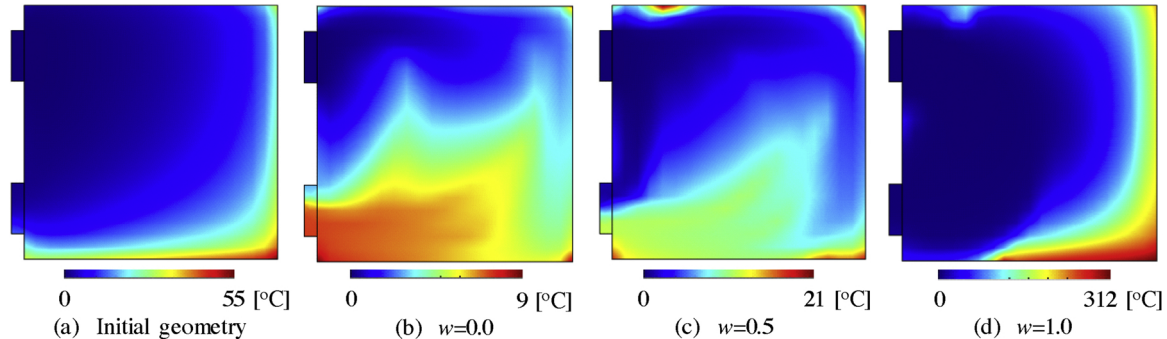
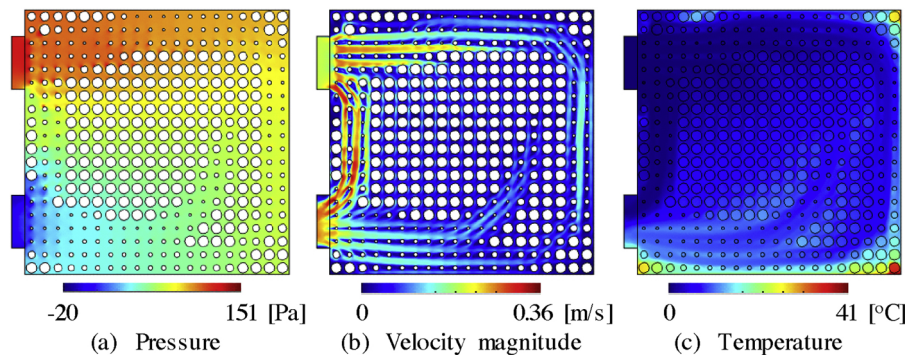


Fig. 14. Temperature distributions of optimal results of the 2D example.

Fig. 15. Analysis results by full scale geometry of the results of the 2D example when $w = 0.5$. (a) Pressure distribution, (b) Velocity distribution and (c) Temperature distribution. (a), (b), and (c) correspond to Figs. 12(c), 13(c), 14(c) respectively.

relative optimization is possible even in the Brinkman–Forchheimer model. One possible reason for the error could be the mutual effect of adjunct lattices. Only a single cell was considered in the derivation of the 2D permeability and form drag coefficient in Fig. 5. However, the flow shape in the lattice array can depend on the adjunct lattices.

Moreover, because the lattice shape varies in each location, such effects can be large. A detailed discussion is shown in Appendix B.

Finally, to verify the effect of the second order form drag term in Eq. (2), we perform the same optimization after removing this term. In other words, this optimization is based on the conventional Darcy's

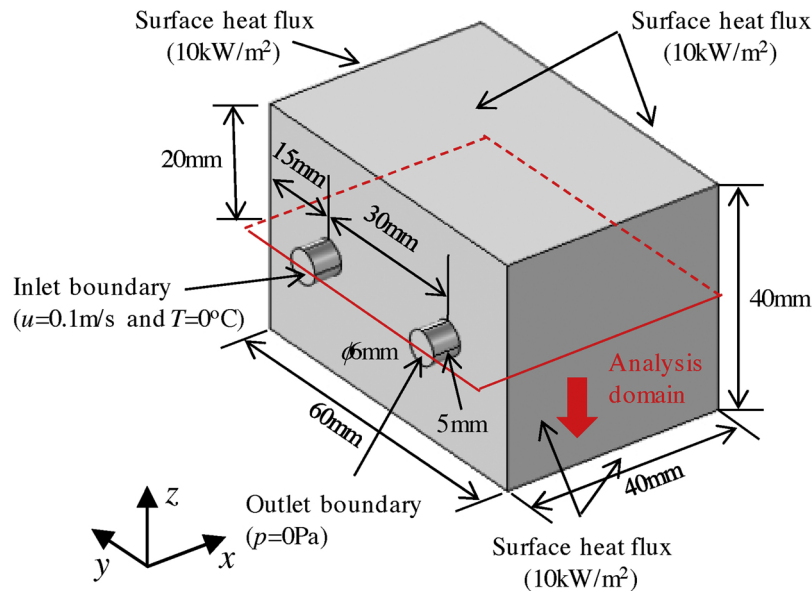


Fig. 16. Analysis domain of 3D numerical example.

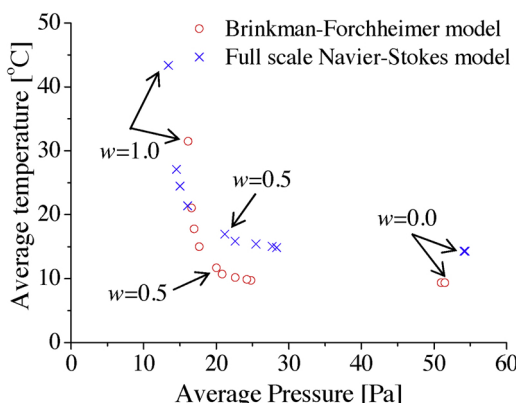


Fig. 17. Pareto solution set of the 3D example of the Brinkman-Forchheimer model and the full scale Navier-Stokes model.

theory. As the flow speed is clearly beyond the limitation imposed under this theory, the error in the pressure approximation reaches 82.5% on average compared to that of the full scale Navier-Stokes models. Full scale analysis results of the optimal solutions are plotted in Fig. 10. Their Pareto front was clearly inferior to that of the full scale analysis of the Brinkman-Forchheimer-based optimal solutions. The temperatures are similar, although the average pressure in the optimal results was 104.2% higher than that of Brinkman-Forchheimer-based method. This comparison shows that the second order drag term in Eq. (2) certainly plays an important role in optimizing the lattice density for Reynolds number up to 10^2 order.

3.2. 3D example

A 3D example is then examined. Fig. 16 shows a target design domain composed of a rectangular lattice domain and two pillar fluid domains corresponding to the inlet and outlet. The lattice domain is entirely filled with lattices shown in Fig. 3(b). Considering the symmetry, only the bottom half of the domain is analyzed. The analysis

domain is divided into a lattice with 5 mm spacing. Thus, the lattice and design domain number is $8 \times 12 \times 4 = 384$. As in the 2D example, the inlet and outlet are on the same side. The rest of the area on the inlet-outlet surface is thermally insulated. A uniform heat flux of 10 kW/m^2 is applied to the other surfaces. The objective function considers the average water pressure at the inlet and average temperature of the heat flux applied to the surface. The lower volume limit is 60% of the volume of the fully dense lattice domain. The initial shape is a uniform lattice with a 60% volume fraction, whose diameter is 3.2 mm. The weight w in the objective function Eq. (5) is made to vary in the range from 0 to 1 in intervals of 0.1.

Fig. 17 shows optimal pressure and temperature distributions after 50 iterations. Volume constraints were active in all results as in the 2D example. Tradeoffs are observed between both criteria in the solutions. We consider $w=0$, 0.5, and 1.0 as representative results. Fig. 18 shows the initial optimal diameter distributions as well as the optimal diameter distributions for the aforementioned values of w , as well as their corresponding full scale geometries. The maximum Reynolds numbers calculated from the Darcy velocity and permeability distributions were 113.2, 77.0, and 80.8 for $w = 0$, 0.5, and 1.0, respectively. As in the 2D case, the path between the inlet and outlet was blocked by a dense lattice for $w = 0$ and 0.5, while it was open for $w = 1.0$.

Figs. 19–21 show the pressure distributions, streamlines and the temperature distributions of the Brinkman-Forchheimer model for the initial geometry and each optimal result. All optimal results avoided high pressure concentration near inlet. From the streamlines, we conclude that the water flow did not reach the bottom right side in the uniform initial lattice. For both $w = 0$ and 0.5, the flow extends to the whole domain. Of course, $w = 0$ covers a wider domain. From the stream-line and temperature distribution, we see that no flows directly cause high temperatures. Temperatures for the uniform and $w = 1.0$ lattices became highly uniform on the right and far side while only a localized high value of temperature was observed for $w = 0$ and 0.5. This confirms that water flow and cooling can be optimized even in the 3D model.

Every result was re-analyzed using the full scale conventional Navier-Stokes and thermal conduction-convection models as in the 2D example. The calculated pressure and temperature are plotted in Fig. 22 together with the Brinkman-Forchheimer results. Both temperature and

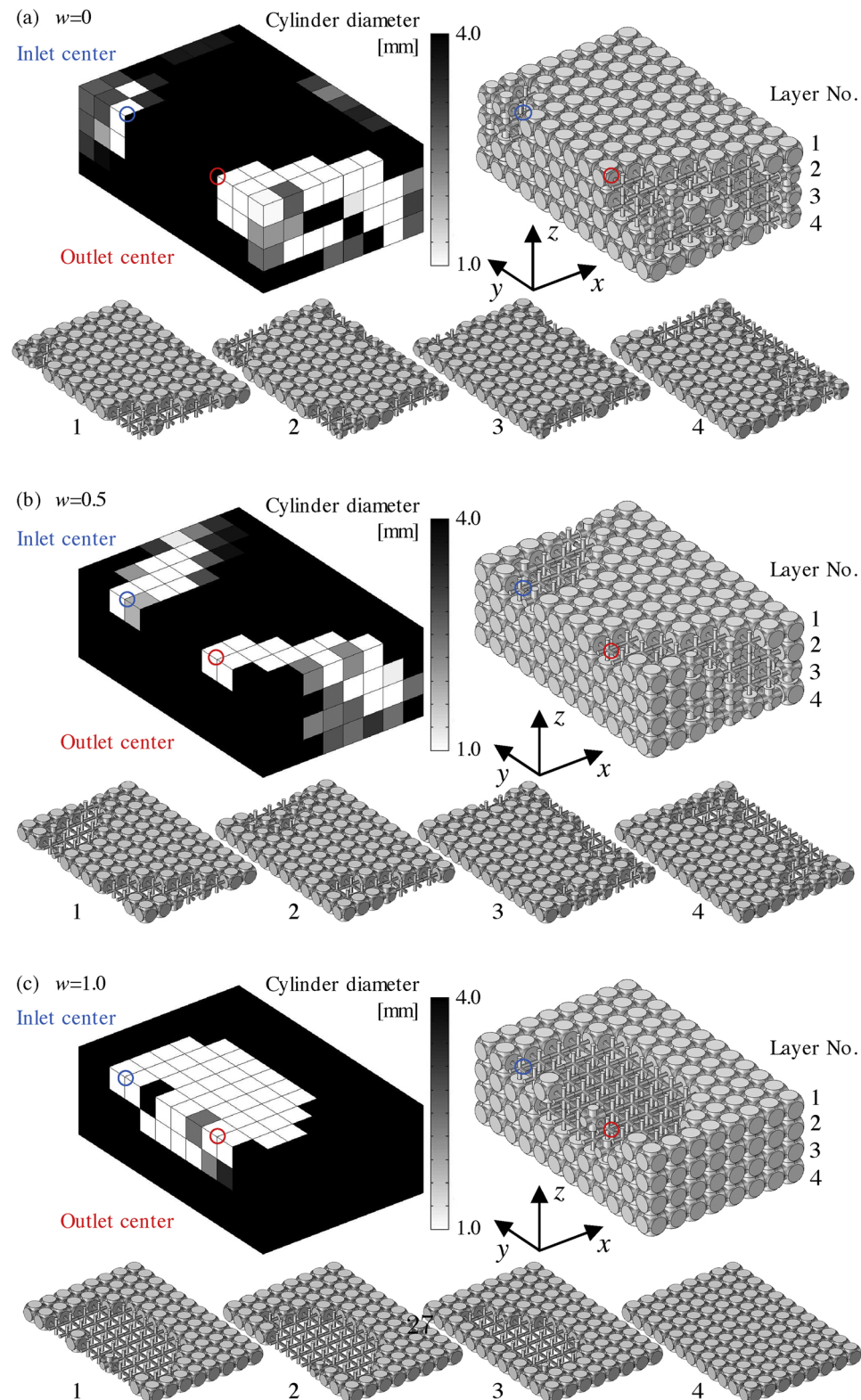


Fig. 18. Optimal diameter distributions and the corresponding geometries of the 3D example.

pressure show similar errors in the 2D case. The pressure and temperatures errors are 10.7% and 31.1%, respectively. Due to the slower inlet velocity, the pressure error is lower than that in the 2D cases. Since inferior-to-superior relationships of each optimal solution held between both models as in the 2D cases, the Brinkman–Forchheimer model can

be used for relative optimization of lattice flow and thermal design, even in 3D cases. Fig. 22 shows pressure, velocity magnitude, and temperature distributions in the full scale model for $w = 0.5$. Fig. 22 shows a distribution similar to that derived from the Brinkman–Forchheimer model.

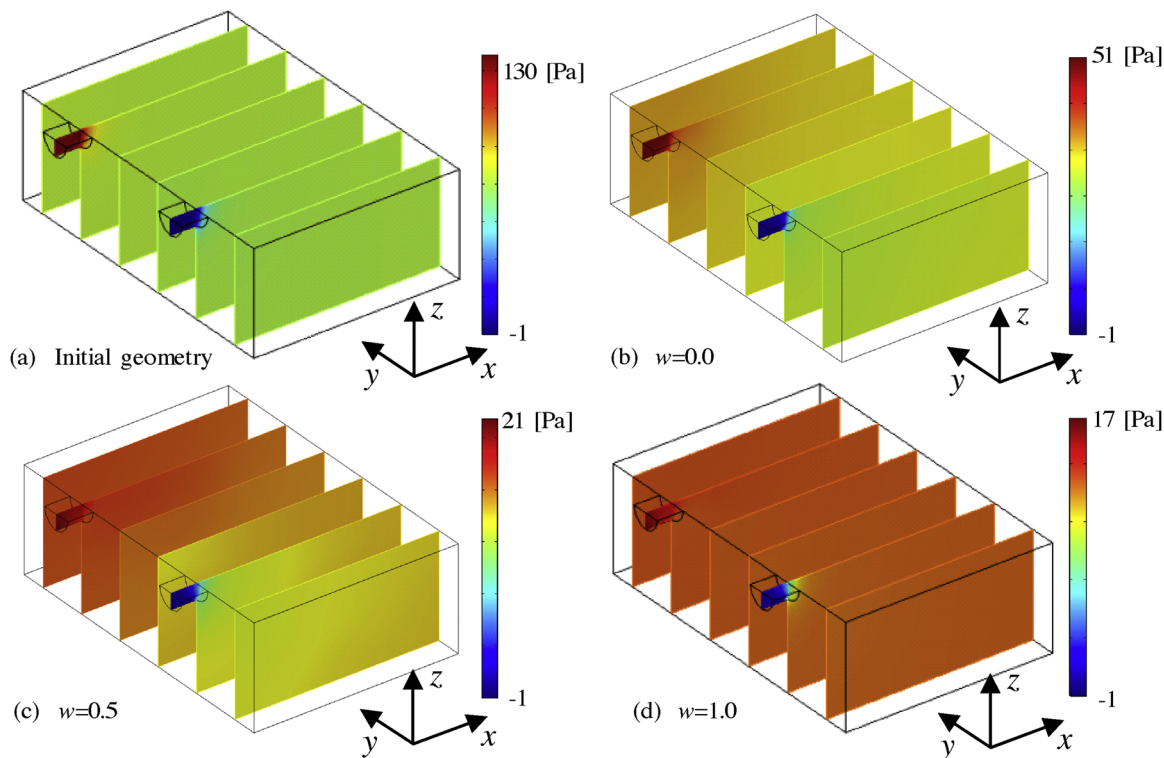


Fig. 19. Pressure distributions of the optimal results of the 3D example.

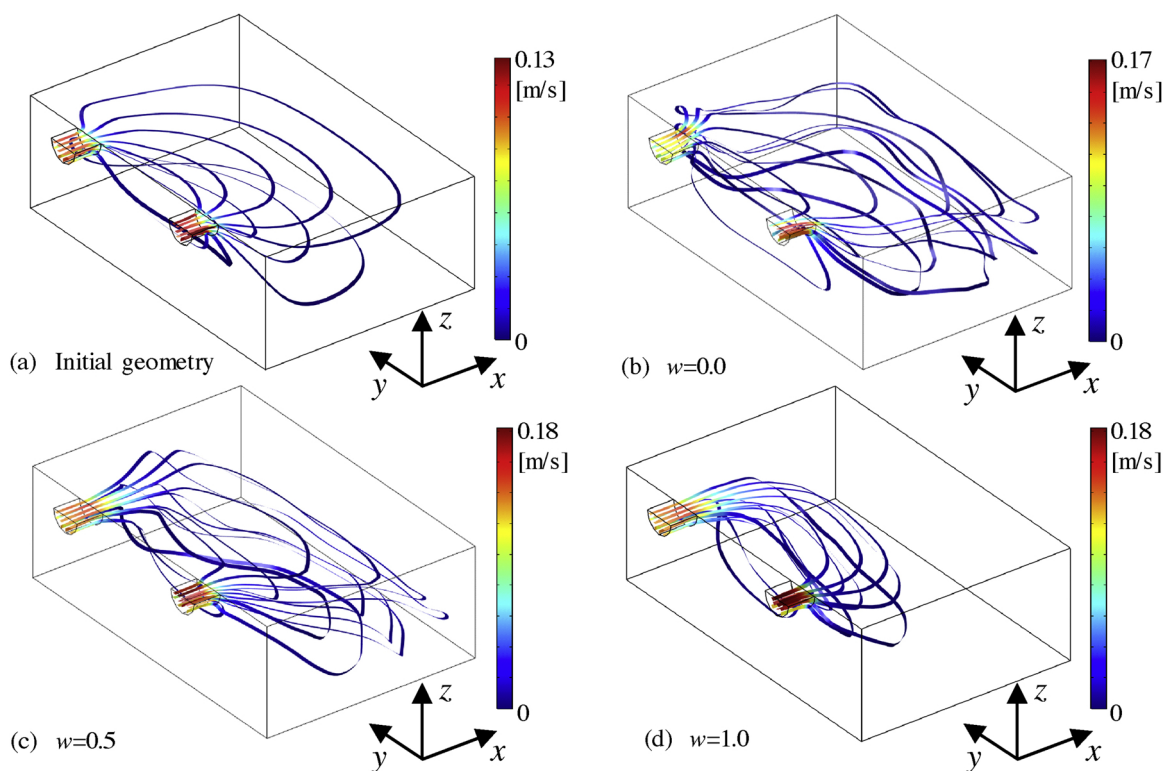


Fig. 20. Stream lines of the optimal results of the 3D example.

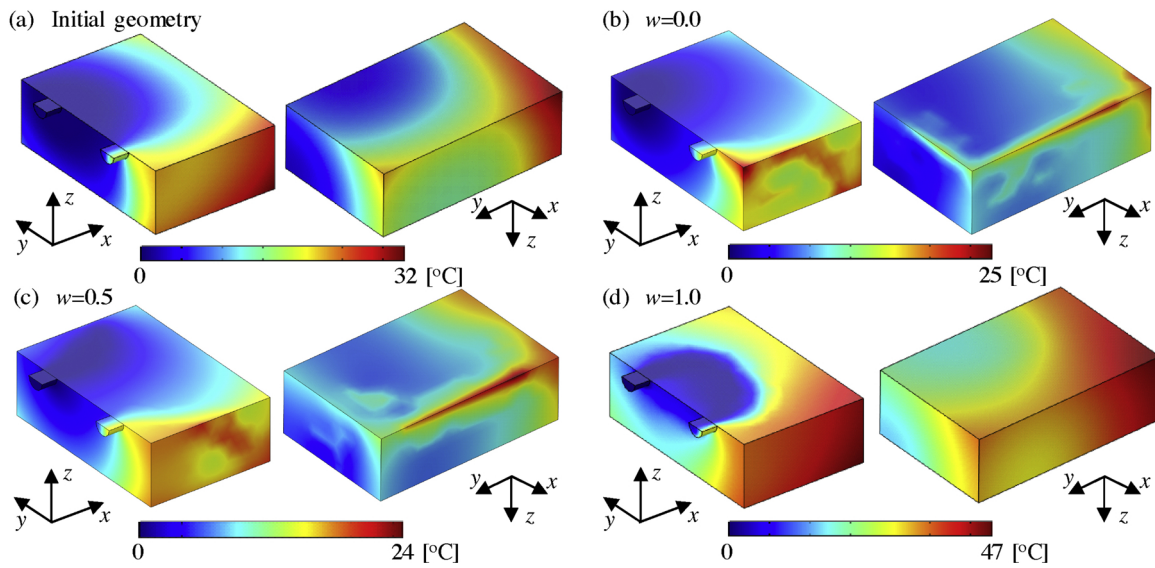
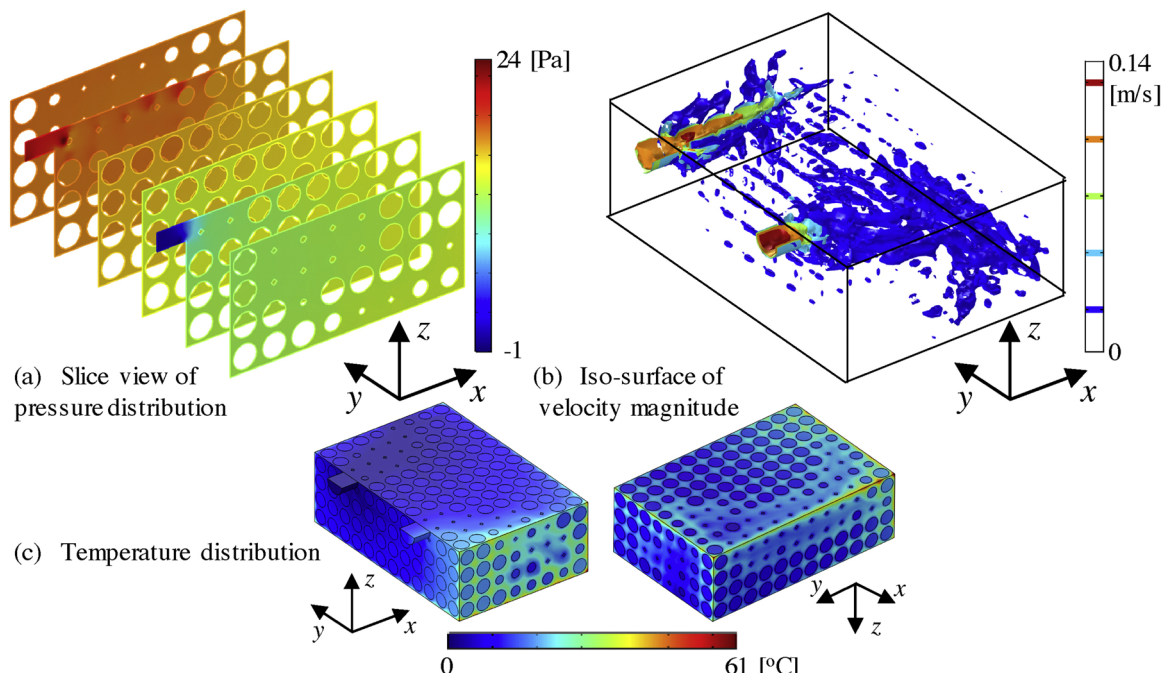


Fig. 21. Temperature distributions of optimal results of 3D example.

Fig. 22. Analysis of results by full scale geometry of the $w = 0.5$ result in the 3D example. (a) Slice view of pressure distribution, (b) Iso-surface of the velocity distribution and (c) Temperature distribution. (a), (b), and (c) correspond to Figs. 19(c), 20(c), 21(c) respectively.

We finally illustrate the practical usefulness of the optimized lattice simulating the time-transient cooling behavior of a hot object. A 2 mm thickness 700 °C Aluminum box with 2700 kg/m³ mass density, 900 J/(kg·K) specific heat and 230 W/(m·K) thermal conductivity is set on the surface of the full scale models of $w = 0.5$ optimal and initial structures of 3D example model. The ambient and coolant temperatures were set to 20 °C. The pressure was set equal to 100 Pa at the inlet, assuming the coolant is driven by a pressure-controlled pump. Fig. 23 shows the temporal behavior of the average temperature in the aluminum shell domains. The optimal lattice was found to cool faster than the

unoptimized lattice.

Fig. 24 shows a carbon steel object additively manufactured by selective laser melting of an optimal lattice with an additional 1 mm outer shell. We finally confirmed that an optimal lattice designed with the proposed method can be fabricated by metallic AM.

4. Conclusion

We have developed a method of optimizing a lattice distribution for effective cooling with coolant flow. Fluid flow through the lattice is

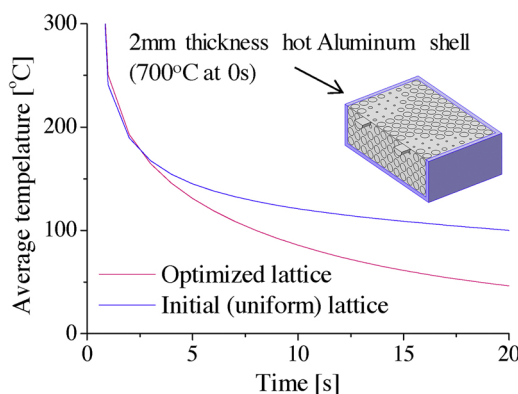


Fig. 23. Temporal history of the average temperature of the outer aluminum shell domain in the transient analysis.

approximated by the Brinkman–Forchheimer equation. The lattice is structured as a combination of simple pillars. We calculated the effective performance of the representative unit lattice using the averaging theorem and the Darcy–Forchheimer law. Polynomials were used to approximate continuous functions that related the design variable to the effective properties. The objective function was a weighted sum of the steady-state pressure loss and average temperature, and was constrained to the lower volume limit of the structure.

The validity of the proposed methodology was confirmed using 2D and 3D examples. Moreover, an inferior-to-superior relationship held, even in the full scale FEM calculation. Thus, our method provides relative optimization. However, certain errors were observed between the

approximate and full scale models, although their distributions were similar. Further study on fluid flow is required because such an error primarily results from imperfections in the fluid-flow approximation in this model. One of the possible reason is the mutual effect of the adjunct lattices. The flow mode change due to the adjunct cell is not considered in the effective properties derived based on the Darcy–Forchheimer law. The accuracy of the results from the approximate Brinkman–Forchheimer equation can be improved by defining the effective properties to be anisotropic.

While this research only evaluated steady-state cooling performance under a uniform heat flux, other aspects such as stiffness, strength, and transient cooling performance must be considered when studying actual heat-exchange devices such as die-casting molds. Objective functions should be varied according to such demands in future research. Experimental verification is also required to show the applicability of each proposed method.

Although the acceptable Reynolds number was increased to the order of 10^2 from past research, the flow can still be slow in the event of rapid cooling. We intend to study the effect of this limitation on practical applications in future work.

Conflict of interest

The authors declare no conflicts of interest.

Acknowledgements

The authors are grateful to X. Ma and R. Moritoyo for their help with computations. This work was supported by Knowledge Hub Aichi, a Priority Research Project of the Aichi Prefectural Government.

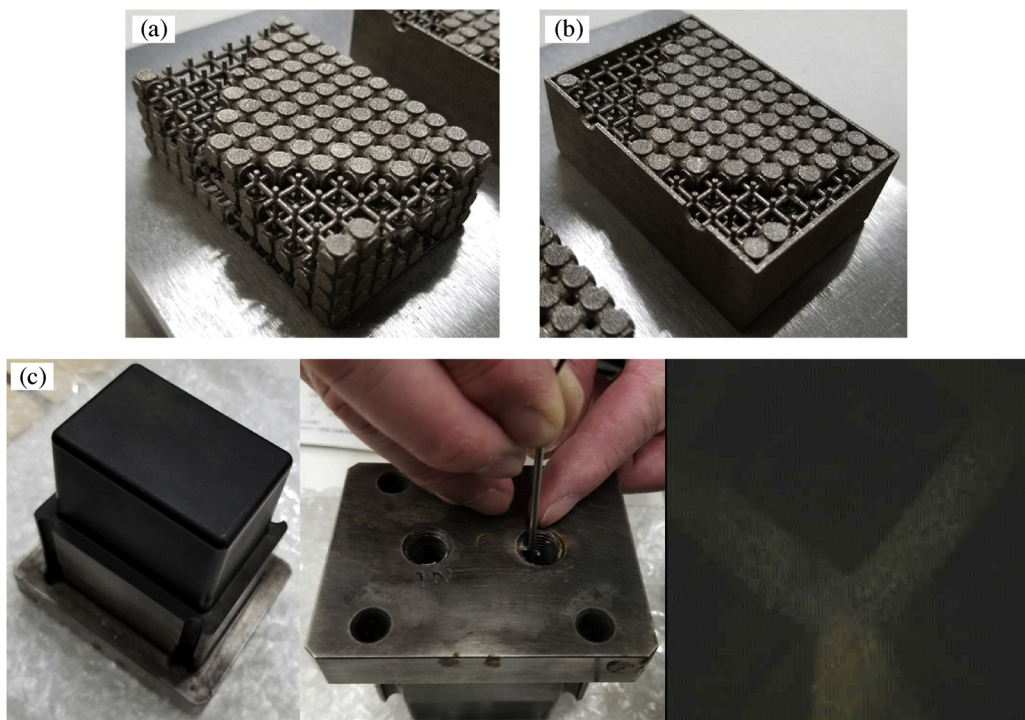


Fig. 24. An optimal lattice fabricated by metal additive manufacturing. (a) Original lattice structure. (b) Lattice structure with 1 mm shell. (c) Lattice embedded casting die sample and observation of the internal structure with an endoscope. (This optimal shape is different from the final version shown in this paper.)

Appendix A. Comparison with a conventional approximation for tube banks

In the first Appendix, we compare our interpolations of the 2D permeability and form drag coefficient in Fig. 6 to confirm their validity with other approximate methods for describing the pressure drop. A traditional approach for predicting the pressure drop due to an object uses the dimensionless Euler number Eu to characterize energy losses as follows:

$$\Delta p = \text{Eu} \frac{\rho U^2}{2} \quad (\text{A.1})$$

where U is the usual flow velocity (not Darcy). Our lattice layout corresponds to the “in-line” layout of tube banks, and data on its Euler number is shown in Ref. [48]. Fig. A.25 shows a comparison between the pressure drops due to the single layer lattice obtained from Darcy–Forchheimer theory in Eq. (2) with the interpolation shown in Fig. A.25, which includes the approximation with the Euler number in Eq. (A.1) and FEM in several lattice pillar diameters. The unit lattice size is 5 mm and the Darcy flow speed is fixed to 0.1 m/s. Although the error between the approximations from Darcy–Forchheimer theory and the Euler number when $D = 2.5$ mm are approximately 40%, the observed trend is consistent.

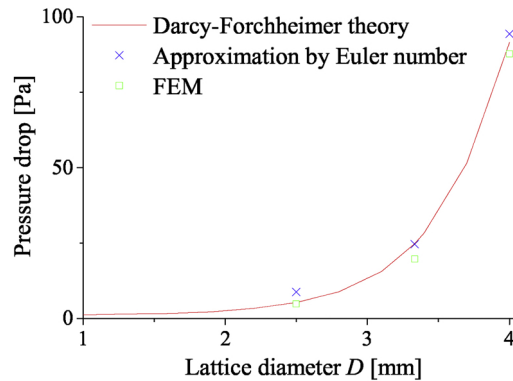


Fig. A.25. Comparison of pressure drops calculated from Darcy–Forchheimer theory, approximated by the Euler number and FEM.

Appendix B. Study on the mutual effect of adjunct lattice cells

One possible reason for the error between the Brinkman–Forchheimer equation and the results from the full scale Navier–Stokes equation is the mutual effect of adjunct lattices. The relationships between the pressure gradient and the Darcy flow are only considered in a single lattice when deriving the permeability and form drag coefficient in Fig. 5. However, the flow shape in the lattice array depends on adjunct lattices. Moreover, such an effect can be large because the lattice shape varies in each location. Fig. A.26 shows the model used in this study. We define a pair of lattices and applied the pressure boundary condition on both sides. We then searched the inlet pressure that generates the Darcy velocity $u = 0.1$ by using an inverse analysis. The obtained inlet pressure is regarded as the pressure drop through the pair of lattices corresponding to a Darcy velocity of $u = 0.1$. We consider lattices with $D = 1.0, 2.5$, and 4 mm corresponding to design variables $d = 0, 0.5$, and 1 , respectively. These lattices are set to the first and second lattices. For reference, the error between the Darcy–Forchheimer approximation and the full scale FEM results in the single lattice cell analysis were 7.1%, 8.1%, and 4.3% when $D = 1.0, 2.5$, and 4 mm, respectively.

Table B.2 summarizes the error in the Brinkman–Forchheimer equation over the results from the Navier–Stokes equation. When the diameter of the first lattice was equal to or larger than the second lattice, the pressure drop calculated from the Navier–Stokes equation was lower than that from the Brinkman–Forchheimer equation. The flow was branched by the first cell and the second cell did not significantly interfere with the flow, as shown in Fig. A.27(b) and (c). Such an effect cannot be described by the Brinkman–Forchheimer equation, thus it generates a higher pressure drop. However, when the first cell diameter is smaller than the second one, the error from the Brinkman–Forchheimer equation is smaller than in the above

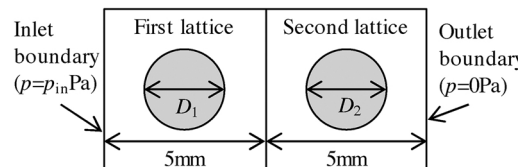


Fig. A.26. Analysis domain for the study of the mutual effect of adjunct lattices.

Table B.2

Pressure drop errors calculated with the Brinkman–Forchheimer equation over the results from the full scale Navier–Stokes equation [%].

D_1 (mm)	D_2 (mm)		
	1.0	2.5	4.0
1.0	73.8	−49.9	−26.8
2.5	108.1	66.3	−17.0
4.0	19.2	26.4	60.5

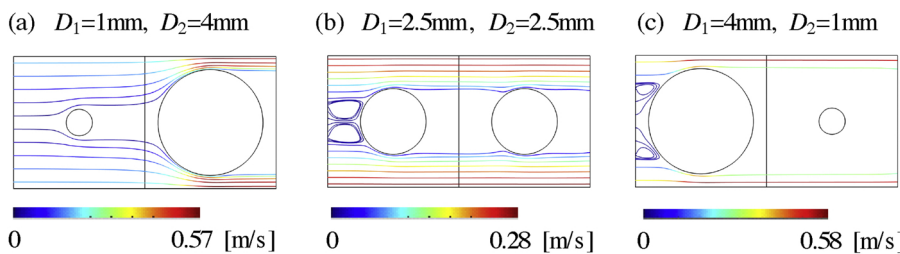


Fig. A.27. Stream lines of the flow through the pair of lattices.

case because the first and second cells interfere with the flow, even in the Navier–Stokes equation model, as shown in Fig. A.27(a). Such a difference can be one reason for the error between the Brinkman–Forchheimer models compared to the Navier–Stokes models shown in Figs. 10 and 17.

References

- [1] I. Gibson, D. Rosen, B. Stucker, *Additive Manufacturing Technologies*, Springer, 2010.
- [2] M. Wong, S. Tsopanos, C.J. Sutcliffe, I. Owen, Selective laser melting of heat transfer devices, *Rapid Prototyp. J.* 13 (5) (2007) 291–297.
- [3] M. Wong, I. Owen, C.J. Sutcliffe, A. Puri, Convective heat transfer and pressure losses across novel heat sinks fabricated by selective laser melting, *Int. J. Heat Mass Transf.* 52 (1–2) (2009) 281–288.
- [4] E.M. Dede, S.N. Joshi, F. Zhou, Topology optimization, additive layer manufacturing, and experimental testing of an air-cooled heat sink, *ASME J. Mech. Des.* 137 (11) (2015) 111403.
- [5] J. Alexandersen, O. Sigmund, N. Aage, Large scale three-dimensional topology optimisation of heat sinks cooled by natural convection, *Int. J. Heat Mass Transf.* 100 (2016) 876–891.
- [6] B.S. Lazarov, O. Sigmund, K.E. Meyer, J. Alexandersen, Experimental validation of additively manufactured optimized shapes for passive cooling, *Appl. Energy* 226 (2018) 330–339.
- [7] M.P. Bendsoe, N. Kikuchi, Generating optimal topologies in structural design using a homogenization method, *Comput. Methods Appl. Mech. Eng.* 71 (2) (1988) 197–224.
- [8] M.P. Bendsoe, O. Sigmund, *Topology Optimization: Theory, Methods, and Applications*, Springer-Verlag, Berlin, 2003.
- [9] S.J. Hollister, Porous scaffold design for tissue engineering, *Nat. Mater.* 4 (7) (2005) 518–524.
- [10] Y. Koizumi, A. Okazaki, A. Chiba, T. Kato, A. Takezawa, Cellular lattices of biomedical Co-Cr-Mo-alloy fabricated by electron beam melting with the aid of shape optimization, *Addit. Manuf.* 12B (2016) 305–313.
- [11] A. Takezawa, Y. Koizumi, M. Kobashi, High-stiffness and strength porous maraging steel via topology optimization and selective laser melting, *Addit. Manuf.* 18 (2017) 194–202.
- [12] A. Takezawa, M. Kobashi, Y. Koizumi, M. Kitamura, Porous metal produced by selective laser melting with effective isotropic thermal conductivity close to the Hashin-Shtrikman bound, *Int. J. Heat Mass Transf.* 105 (2017) 564–572.
- [13] J. Schwerdtfeger, F. Wein, G. Leugering, R.F. Singer, C. Körner, M. Stingl, F. Schury, Design of auxetic structures via mathematical optimization, *Adv. Mater.* 23 (22–23) (2011) 2650–2654.
- [14] E. Andreassen, B.S. Lazarov, O. Sigmund, Design of manufacturable 3d extremal elastic microstructure, *Mech. Mater.* 69 (1) (2014) 1–10.
- [15] A. Clausen, F. Wang, J.S. Jensen, O. Sigmund, J.A. Lewis, Topology optimized architectures with programmable Poisson's ratio over large deformations, *Adv. Mater.* 27 (37) (2015) 5523–5527.
- [16] A. Takezawa, M. Kobashi, M. Kitamura, Porous composite with negative thermal expansion obtained by photopolymer additive manufacturing, *APL Mater.* 3 (7) (2015) 076103.
- [17] A. Takezawa, M. Kobashi, Design methodology for porous composites with tunable thermal expansion produced by multi-material topology optimization and additive manufacturing, *Compos. B Eng.* 131 (2017) 21–29.
- [18] Y.M. Xie, X. Yang, J. Shen, X. Yan, A. Ghaedizadeh, J. Rong, X. Huang, S. Zhou, Designing orthotropic materials for negative or zero compressibility, *Int. J. Solid Struct.* 51 (23) (2014) 4038–4051.
- [19] Y. Miyamoto, W.A. Kaysser, B.H. Rabin, A. Kawasaki, R. Ford, *Functionally Graded Materials: Design, Processing and Applications*, Springer Science & Business Media, 2013.
- [20] S.A. Khanoki, D. Pasini, Multiscale design and multiobjective optimization of orthopedic hip implants with functionally graded cellular material, *J. Biomech. Eng.* 134 (3) (2012) 031004.
- [21] P. Zhang, J. Toman, Y. Yu, E. Biyikli, M. Kirca, M. Chmielus, A.C. To, Efficient design-optimization of variable-density hexagonal cellular structure by additive manufacturing: Theory and validation, *ASME J. Manuf. Sci. Eng.* 137 (2) (2015) 021004.
- [22] L. Cheng, J. Bai, A.C. To, Functionally graded lattice structure topology optimization for the design of additive manufactured components with stress constraints, *Comput. Methods Appl. Mech. Eng.* 344 (2019) 334–359.
- [23] C.L.M.E. Lynch, M.T.A. Mordasky, Design, testing, and mechanical behavior of additively manufactured casing with optimized lattice structure, *Addit. Manuf.* 22 (2018) 462–471.
- [24] A. Clausen, N. Aage, O. Sigmund, Exploiting additive manufacturing infill in topology optimization for improved buckling load, *Engineering* 2 (2) (2016) 250–257.
- [25] X. Wang, P. Zhang, S. Ludwick, E. Belski, A.C. To, Natural frequency optimization of 3d printed variable-density honeycomb structure via a homogenization-based approach, *Addit. Manuf.* 20 (2018) 189–198.
- [26] L. Cheng, X. Liang, E. Belski, X. Wang, J.M. Sietins, S. Ludwick, A. To, Natural frequency optimization of variable-density additive manufactured lattice structure: theory and experimental validation, *J. Manuf. Sci. Eng.* 140 (10) (2018) 105002.
- [27] L. Cheng, J. Liu, X. Liang, A.C. To, Coupling lattice structure topology optimization with design-dependent feature evolution for additive manufactured heat conduction design, *Comput. Methods Appl. Mech. Eng.* 332 (2018) 408–439.
- [28] L. Cheng, J. Liu, A.C. To, Concurrent lattice infill with feature evolution optimization for additive manufactured heat conduction design, *Struct. Multidisc. Optim.* (2018) 1–25.
- [29] J.K. Guest, J.H. Prévost, Optimizing multifunctional materials: design of microstructures for maximized stiffness and fluid permeability, *Int. J. Solid Struct.* 43 (22) (2006) 7028–7047.
- [30] J.K. Guest, J.H. Prévost, Design of maximum permeability material structures, *Comput. Methods Appl. Mech. Eng.* 196 (4–6) (2007) 1006–1017.
- [31] V.J. Challis, J.K. Guest, J.F. Grotowski, A.P. Roberts, Computationally generated cross-property bounds for stiffness and fluid permeability using topology optimization, *Int. J. Solid Struct.* 49 (23–24) (2012) 3397–3408.
- [32] T. Borrvall, J. Petersson, Topology optimization of fluids in stokes flow, *Int. J. Numer. Methods Fluid* 41 (1) (2003) 77–107.
- [33] L.H. Olesen, F. Okkels, H. Bruus, A high-level programming-language implementation of topology optimization applied to steady-state navier-stokes flow, *Int. J. Numer. Methods Eng.* 65 (7) (2006) 975–1001.
- [34] A.A. Koga, E.C.C. Lopes, H.F.V. Nova, C.R. de Lima, E.C.N. Silva, Development of heat sink device by using topology optimization, *Int. J. Heat Mass Transf.* 64 (2013) 759–772.
- [35] G.H. Yoon, Topology optimization for turbulent flow with spalart-allmaras model, *Comput. Methods Appl. Mech. Eng.* 303 (2016) 288–311.
- [36] J.C. Ward, Turbulent flow in porous media, *J. Hydraul. Div.* 90 (5) (1964) 1–12.
- [37] D.A. Nield, A. Bejan, *Convection in Porous Media*, Springer, New York, 2013.
- [38] L. Weber, D. Ingram, S. Guardia, A. Athanasiou-Ioannou, A. Mortensen, Fluid flow through replicated microcellular materials in the Darcy-Forchheimer regime, *Acta Mater.* 126 (2017) 280–293.
- [39] A.J. Otaru, H.P. Morvan, A.R. Kennedy, Measurement and simulation of pressure drop across replicated porous aluminium in the Darcy-Forchheimer regime, *Acta Mater.* 149 (2018) 265–273.
- [40] K. Svahnberg, The method of moving asymptotes – a new method for structural optimization, *Int. J. Numer. Methods Eng.* 24 (2) (1987) 359–373.
- [41] D.D. Joseph, D.A. Nield, G. Papanicolaou, Nonlinear equation governing flow in a saturated porous medium, *Water Resour. Res.* 18 (4) (1982) 1049–1052.
- [42] K. Vafai, C.L. Tien, Boundary and inertia effects on flow and heat transfer in porous media, *Int. J. Heat Mass Transf.* 24 (2) (1981) 195–203.
- [43] K. Vafai, C.L. Tien, Boundary and inertia effects on convective mass transfer in porous media, *Int. J. Heat Mass Transf.* 25 (8) (1982) 1183–1190.
- [44] C.T. Hsu, P. Cheng, Thermal dispersion in a porous medium, *Int. J. Heat Mass Transf.* 33 (8) (1990) 1587–1597.
- [45] R. Hill, On constitutive macro-variables for heterogeneous solids at finite strain, *Proc. R. Soc. Lond. Math. Phys. Sci.* 326 (1972) 131–147.
- [46] Z. Hashin, Analysis of composite materials – a survey, *J. Appl. Mech.* 50 (3) (1983) 481–505.
- [47] G. Allaire, *Shape Optimization by the Homogenization Method*, Springer-Verlag, New York, 2001.
- [48] E.U. Schlunder, *Heat Exchanger Design Handbook*, Hemisphere Publishing, New York, 1983.
- [49] E.J. Haug, K.K. Choi, V. Komkov, *Design Sensitivity Analysis of Structural Systems*, Academic Press, Orlando, 1986.